Published OnlineFirst September 12, 2014; DOI: 10.1158/0008-5472.CAN-14-1656

Cancer Research

Targeted Noninvasive Imaging of EGFR-Expressing Orthotopic Pancreatic Cancer Using Multispectral Optoacoustic Tomography

Shanice V. Hudson, Justin S. Huang, Wenyuan Yin, et al.

Cancer Res 2014;74:6271-6279. Published OnlineFirst September 12, 2014.

Published OnlineFirst September 12, 2014; DOI: 10.1158/0008-5472.CAN-14-1656

Therapeutics, Targets, and Chemical Biology

Cancer Research

Targeted Noninvasive Imaging of EGFR-Expressing Orthotopic Pancreatic Cancer Using Multispectral Optoacoustic Tomography

Shanice V. Hudson[1], Justin S. Huang[1], Wenyuan Yin[1], Sabrin Albeituni[1], Jamie Rush[2], Anil Khanal[1], Jun Yan[1], Brian P. Ceresa[2], Hermann B. Frieboes[2,3], and Lacey R. McNally[1,2]

Abstract

Detection of orthotopic xenograft tumors is difficult due to poor spatial resolution and reduced image fidelity with traditional optical imaging modalities. In particular, light scattering and attenuation in tissue at depths beyond subcutaneous implantation hinder adequate visualization. We evaluate the use of multispectral optoacoustic tomography (MSOT) to detect upregulated epidermal growth factor (EGF) receptor in orthotopic pancreatic xenografts using a near-infrared EGF-conjugated CF-750 fluorescent probe. MSOT is based on the photoacoustic effect and thus not limited by photon scattering, resulting in high-resolution tomographic images. Pancreatic tumor-bearing mice with luciferase-transduced S2VP10L tumors were intravenously injected with EGF-750 probe before MSOT imaging. We characterized probe specificity and bioactivity via immunoblotting, immunocytochemistry, and flow cytometric analysis. *In vitro* data along with optical bioluminescence/fluorescence imaging were used to validate acquired MSOT *in vivo* images of probe biodistribution. Indocyanine green dye was used as a nonspecific control to define specificity of EGF-probe accumulation. Maximum accumulation occurred at 6 hours postinjection, demonstrating specific intratumoral probe uptake and minimal liver and kidney off-target accumulation. Optical bioluminescence and fluorescence imaging confirmed tumor-specific probe accumulation consistent with MSOT images. These studies demonstrate the utility of MSOT to obtain volumetric images of ligand probe biodistribution *in vivo* to detect orthotopic pancreatic tumor lesions through active targeting of the EGF receptor. *Cancer Res; 74(21); 6271–9. ©2014 AACR.*

Introduction

Early detection of cancer—a critical parameter affecting overall survival—can be difficult using current imaging modalities. In particular, pancreatic cancer is notorious for avoiding detection until after the onset of systemic disease. While subcutaneously engrafted models of pancreatic cancer are frequently used, the translational superiority of orthotopic models necessitates their use for clinically relevant investigations (1). In particular, imaging of orthotopic pancreatic tumors in preclinical models is essential for monitoring of tumor burden and characterization of tumor activity. Traditional nuclear imaging has limitations depending on the modality used, which include poor spatial resolution, low sensitivity, ionizing radiation, or lack of 3D anatomic context (2). Multimodality imaging techniques integrating anatomic visualization with molecular imaging, such as SPECT/CT and PET/CT are capable of 3D nuclear imaging. However these systems are hindered by decreased sensitivity, low resolution at increased depths, and long acquisition times, making them less practical for investigating real-time molecular event dynamics *in vivo* (3).

Bioluminescence and fluorescence imaging suffer from light scattering and absorption, as well as poor resolution at depth when compared with computed tomography (CT) and magnetic resonance imaging (MRI; ref. 4). Optoacoustic (photoacoustic) imaging is an emerging technology with many desirable characteristics as an imaging modality; it uses nonionizing electromagnetic waves, offers high spatial resolution, and sensitivity (5). Optoacoustic imaging is unique in that it resolves optical contrast, but the resolution obeys the rules of ultrasonic diffraction; therefore, optoacoustic methods render photon scattering irrelevant to image formation, enabling the capability for novel high-resolution insights into the biologic function of entire tumors, organs, and systems (6). Optoacoustic tomography has higher spatial resolution and deeper imaging depth because scattering of the ultrasonic signal in tissue is much weaker than for optical signals. The development of imaging probes for use in optoacoustic tomography is essential to fully leverage the capabilities of this technology for cancer detection in living subjects (7–10).

[1]Department of Medicine, University of Louisville, Kentucky. [2]Department of Pharmacology and Toxicology, University of Louisville, Kentucky. [3]Department of Bioengineering, University of Louisville, Kentucky.

Note: Supplementary data for this article are available at Cancer Research Online (http://cancerres.aacrjournals.org/).

S.V. Hudson and J.S. Huang contributed equally to this article.

Corresponding Author: Lacey R. McNally, Department of Medicine, 505 S Hancock, CTR 307, Louisville, KY 40202. Phone: 502-852-2288; Fax: 502-852-2123; E-mail: lrmcna01@louisville.edu

doi: 10.1158/0008-5472.CAN-14-1656

Published OnlineFirst September 12, 2014; DOI: 10.1158/0008-5472.CAN-14-1656

Because epithelial growth factor receptor (EGFR) is overexpressed in many cancers, including pancreatic lesions, labeled EGF probes have been used to investigate EGFR activation, receptor–ligand complex endocytic trafficking and sorting (11–13), and EGFR expression in breast, head and neck, and pancreatic cancer xenografts (14–16).

Here, we evaluate the ability to detect orthotopic pancreatic tumors through optoacoustic tomography using an EGF ligand–conjugated fluorescent near-infrared (NIR) probe as a contrast agent. We comprehensively characterized the EGF-750 probe with a battery of *in vitro* assays to verify its bioactivity and specificity before *in vivo* analysis. Accumulation of EGF-750 probe within the primary solid tumor was assessed by multispectral optoacoustic tomography (MSOT). Western immunoblotting and flow cytometry results confirm the specific binding depicted by MSOT images. In particular, we evaluate the utility of MSOT for specific and sensitive high-resolution detection of orthotopic pancreatic tumors at depths exceeding 5 mm.

Materials and Methods

Synthesis and characterization of EGF-750 probe

Recombinant human EGF (6222 Dalton, sequence: NSDSECPLSH DGYCLHDGVC MYIEALDKYA CNCVVGYIGE RCQYRDLKWW ELRl; ProSpec) and CF-750 N-hydroxysuccinimide ester amine-reactive dye (Biotium) were conjugated as previously described (17, 18). Briefly, lyophilized EGF was reconstituted in phosphate-buffered saline at pH 7.4 (Dulbecco's PBS; Life Technologies) to a concentration of 2.5 mg/mL. From this EGF polypeptide solution, 5 μg was transferred to a reaction tube for bioconjugation, to which was added 1/10 volume of 1 mol/L sodium bicarbonate solution. Lyophilized CF-750 dye was reconstituted using 10% dimethyl sulfoxide (DMSO; Fisher Scientific) in deionized water. CF-750 dye (100 μL) was conjugated to EGF ligand, resulting in a final concentration of 1 μmol/L EGF-750 probe. All synthesis processes were performed in a dark room due to light sensitivity of the NIR-dye. The mixture was vortexed and then sonicated on ice for 30 minutes followed by dialysis for 16 hours to remove unconjugated excess dye. The EGF-750 probe was dialyzed against phosphate buffer (10 mmol/L, pH 7.4) for three days in the dialysis tube (2000 nominal molecular weight cut-off; Sigma-Aldrich). The phosphate buffer was exchanged eight times during 4-hour time intervals. The optical absorption spectra of both CF-750 NIR dye and EGF probe were collected from a UV-Visible (UV-Vis) spectrophotometer (Cary 100 Bio; Varian).

Cell culture

Metastatic subclones of the SUIT-2 pancreatic adenocarcinoma cell line, S2VP10 and S2CP9, were kindly provided by Dr. Michael A. Hollingsworth at the University of Nebraska (Omaha, Nebraska). Cell lines MiaPaCa-2, PANC-1, HeLa, SKOV3.ip1 (EGFR-positive control; refs. 19–21), NIH/3T3 (EGFR-negative control; refs. 22, 23), and MCF7 were obtained from the American Type Culture Collection (ATCC). Cells were cultured at 37°C and 5% CO_2 in either Dulbecco's modified Eagle medium (DMEM) or Roswell Park Memorial Institute (RPMI)-1640 medium supplemented with 10% fetal bovine serum (FBS; Atlanta Biologicals) and 1% L-glutamine (Gibco).

Western blot analysis

EGFR expression was determined by Western blotting using standard techniques. Pancreatic cells, S2VP10, S2CP9, MiaPaCa-2, and PANC-1, along with positive control (SKOV3.ip1) and negative controls (MCF7, NIH/3T3) were seeded at a density of 5×10^5 cells per well for 24 hours. Using NP-40 detergent solution (Pierce Biotechnology, Inc., Thermo Scientific), phosphatase and protease inhibitors (Halt Inhibitor Cocktail; Thermo Scientific) in a 200 mmol/L sodium orthovanadate solution, cells were lysed and centrifuged at 13,300 $\times g$ for 10 minutes at 4°C. Total protein was quantified using the Pierce BCA assay (Thermo Scientific). Protein from each cell line was loaded onto NuPage 12% Bis-Tris Novex gel (Invitrogen). Following electrophoresis, proteins were transferred onto nitrocellulose membrane using the iBlot dry blotting system (Life Technologies). The membrane was blocked with 3 mL Li-Cor blocking buffer (Li-Cor) for 30 minutes, then incubated with rabbit anti-EGFR (Abcam) at a concentration of 1:1,000 and mouse anti–β-actin antibody (Thermo Scientific) at 1:5,000. Membranes were incubated overnight at 4°C and then washed three times using Tris-buffered saline and tween 20 (TBST; 50 mmol/L Tris, 150 mmol/L NaCl, and 0.05% Tween 20) and secondary antibodies donkey anti-mouse IRDye 680RD and donkey anti-rabbit IRDye 800CW (Li-Cor) at concentrations of 1:2,000 in blocking buffer for 1 hour. Membranes were then scanned and analyzed using the Li-Cor Odyssey Infrared Imaging System (Li-Cor). Dosimetry was performed using Odyssey software, in which intensity values for EGFR band were divided by the β-actin band to normalize relative signal abundance.

EGF-750 activation of EGFR

Cervical adenocarcinoma HeLa cells were incubated with either EGF (10 ng/mL) or EGF-750 (1, 10, or 100 ng/mL) for 15 minutes at 37°C. Western blotting was performed as previously described (24). Proteins were resuspended in Lamelli sample buffer and resolved by 7.5% SDS-Page gel before transfer onto nitrocellulose membrane. The membrane was blocked with 5% milk and 0.5% TBST buffer. Immunoblots were incubated in TBST with mouse anti-EGFR antibody (Santa Cruz Biotechnology) and rabbit anti-pY1068 phosphorylated-EGFR antibody (Cell Signaling Technology) at concentrations of 1:1,000 and 1:500, respectively; mouse anti-α-tubulin was added at a concentration of 1:5,000 as a control. Membranes were incubated overnight at 4°C then washed three times before incubation at room temperature for 1 hour with blocking buffer (5% milk and 0.5% TBST), anti-mouse and anti-rabbit (Pierce) secondary antibodies conjugated to horseradish peroxidase at concentrations of 1:2,500. Membranes were developed using ECL reagent in a Fotodyne Imager (Fotodyne Inc.).

Immunocytochemistry of EGF-750 probe uptake

Cell lines S2VP10, MiaPaCa-2, and MCF7 (low EGFR expression) were treated with Texas Red–EGF complex (Invitrogen) for observation of ligand binding–induced EGFR trafficking,

Published OnlineFirst September 12, 2014; DOI: 10.1158/0008-5472.CAN-14-1656

and rabbit polyclonal early endosomal antigen-1 antibody (EEA1; Cell Signaling Technology) to visualize endocytosis and intracellular sorting. All cells were grown to confluency on coverslips and then serum-starved for 2 hours before a 10-minute pulse with 2 μg/mL Texas Red–EGF ligand. Following two washes with ice-cold citrate buffer to remove excess extracellular ligand, the 0 and 10-minute treatment groups were immediately fixed in 4% paraformaldehyde for 5 minutes at room temperature, then an additional 15 minutes on ice. The 30-minute treatment group was incubated at 37°C and 5% CO_2 for another 20 minutes before fixation. Coverslips were then washed two times with ice-cold PBS, and then washed three additional times for 5 minutes each using PBS^{++} (0.5 mmol/L magnesium and calcium chloride) before permeabilization in 0.1% saponin, 5% FBS, and PBS for 20 minutes at room temperature, followed by another wash in PBS. Treatment with 1:1,500 EEA1 in saponin for 1 hour preceded another PBS^{++} wash and subsequent 1:250 incubation with anti-rabbit Alexa 488 secondary antibody (Invitrogen) in the dark for 1 hour at 25°C. Coverslips were then washed six times for 10 minutes each with PBS++ and then rinsed with double-distilled H_2O and mounted in Prolong without DAPI (Invitrogen). A Nikon Ti Eclipse immunofluorescence microscope (Nikon) was used to image the coverslips.

Flow cytometry

Cell lines S2VP10L and NIH/3T3 (negative control) were seeded at a density of 4×10^5 cells per well in 22.1-mm plates; Ab-1 wells were blocked for 1 hour with 10 μL anti-EGFR antibody (EMD Millipore) before addition of 20 μL of 1 μmol/L EGF-750 probe. Experimental wells were incubated with probe for 30 minutes, then cells were scraped and washed with PBS. Flow cytometric analysis of probe uptake was conducted using the BD FACSCanto (BD Biosciences). The APC-Cy7 filter setting detected cells positive for bound CF-750 fluorescent dye conjugate. Raw data were analyzed using the FlowJo software (FlowJo).

Orthotopic pancreatic cancer xenografts

Strict adherence to the University of Louisville Institutional Animal Care and Use Committee–approved protocol was maintained throughout the study. Five-week-old female C.B-17 SCID mice (Harlan Laboratories) were acclimated for 1 week before the study. All surgical procedures were performed in a sterile hood. Orthotopic cell implantation was performed as previously described (25); a 1-cm incision was made in the upper left abdominal quadrant and the spleen was used to indirectly position the tail of the pancreas, carefully avoiding direct pancreatic manipulation. Five mice per cohort were injected with 30 μL of either 1.5×10^5 S2VP10L (luciferase clone of high-EGFR-expressing S2VP10 pancreatic cancer cells) or 2.5×10^6 MiaPaCa-2 (low-EGFR–expressing), cells into the tail of the pancreas using a 28-gauge needle. Sterile cotton-tipped applicators were used to cover the injection site for 30 seconds to prevent peritoneal leakage. The organs were reseated in the abdomen before single-layer incision closure with 5-0 nylon sutures. Animals had 30 minutes of postoperative recovery period on a heated pad before being returned to cages supplied with clear, liquid acetaminophen for 24 hours along with food and water *ad libitum*. Confirmation of orthotopic implantation was performed using bioluminescence optical imaging on the Advanced Molecular Imager (AMI-1000X; Spectral Imaging Instruments). Mice with detectable leakage from the pancreas were removed from the study. Mice received intraperitoneal (i.p.) injection of 2.5 mg luciferin bioluminescent substrate (D-luciferin potassium salt; PerkinElmer) 10 minutes before weekly imaging to monitor orthotopic tumor and metastatic growth. Region of interest (ROI) analysis was used to measure the light emitted for orthotopic sites using the AMI Image Viewer software. Sutures were removed 7 days following implantation. Once mice had palpable tumors, mice received i.v. injection of 200 μL of 100 nmol/L EGF-750 probe; control mice for each tumor model received coinjection of indocyanine green (ICG; Sigma-Aldrich). Probe was allowed to accumulate in the tumor for 3 to 24 hours before imaging.

Tumor imaging

The inVision-256TF multispectral optoacoustic tomography system (iThera Medical) was used for real-time imaging of orthotopic pancreatic xenografts. The MSOT data reported here are from S2VP10L-implanted mice imaged at 14 days postimplantation. MiaPaCa-2 control mice were imaged via MSOT at 35 days postimplantation. Mice were anesthetized with 1.6% isoflurane inhalant delivered in 0.8 L medical air and 0.1 L O_2, then depilated using a combination of shaving and application of Nair cream with aloe (Church & Dwight Co.), which was removed with moist gauze. Anesthetic depth was maintained throughout the image acquisitions, with mice oriented ventral side up in the animal holder. Whole-body imaging was performed at 3, 6, and 24-hour intervals using transversal slices with a 0.2-mm step from the liver to the kidney (38–56 mm), at wavelengths of 680, 710, 730, 740, 760, 770, 780, 800, 850, 900 nm for each position, using 25 averages per wavelength with acquisition time of 10 microseconds per frame to minimize the influence of animal movement in the images. Excitation of the EGF-750 probe was conducted using a tunable parametric oscillator pumped by an Nd:YAG laser. The pancreas tumor was identified by a live-feed screen preview multispectral signal (MSP). Optical bioluminescence and fluorescence imaging using the AMI-1000X optical imaging system (Spectral Instruments Imaging) was performed to verify MSOT images of tumor location and EGF-750 probe binding specificity *in vivo*, as well as for monitoring of orthotopic tumor and metastatic growth. Mice were anesthetized with 2% isoflurane in a sealed chamber and then placed with ventral side up on a 37°C staging platform for image acquisition. Mice were i.p. injected with 2.5 mg luciferin 10 minutes before weekly bioluminescence imaging; i.v. injection of EGF-750 probe preceded fluorescence imaging at an excitation of 745 nm and 790 nm. ROI analysis was used to measure fluorescence emitted using the AMI Image Viewer software. Upon completion of imaging protocol, animals were euthanized via carbon dioxide inhalation and pancreas tumor and liver tissues were harvested and imaged *ex vivo* using the AMI-1000X. Control mice were

Published OnlineFirst September 12, 2014; DOI: 10.1158/0008-5472.CAN-14-1656

injected with unconjugated inert CF-750 dye alone to evaluate level of nonspecific binding.

MSOT image reconstruction

Images were reconstructed using the multispectral processing along with ViewMSOT software as previously described (26). Data were optimized using high-resolution (75 μm) backprojection reconstruction with 3D Gaussian filter (size $9 \times 9 \times 3$) homogenization from MATLAB, which was done before applying the multispectral processing using linear regression also from MATLAB. Maximum intensity projections were obtained using MATLAB along with ViewMSOT after reconstruction.

Statistical analysis

Differences in signal mean fluorescence intensity (MFI) of samples measured by flow cytometry were assessed using the Wilcoxon signed-rank test. Statistical analysis was completed with the SAS 9.3 software (SAS Institute). P values ≤ 0.05 were considered to be significant.

Results

EGF-750 characterization

The EGF polypeptide was labeled using an NHS ester, amine-reactive NIR CF-750 dye. Following the conjugation of EGF polypeptide, the absorbance spectrum of the novel EGF-750 probe was compared with that of the free dye, yielding similar absorption patterns with peaks near 750 nm (Fig. 1A), which indicates that bioconjugation did not significantly change the expected absorbance signature of the dye. The degree of labeling (number of CF-750 dye molecules per EGF molecule) was calculated according to the manufacturer's instruction (Biotium) by using an extinction coefficient of 2.85/(M cm) at 280 nm for EGF, and an extinction coefficient of 250,000/(M cm) at 750 nm for CF-750; the degree of labeling was found to be 1.32. Bioactivity of EGF-750 was verified by the dose-dependent induction of EGFR phosphorylation (Fig. 1B). HeLa cells were treated with no ligand, 10 ng/mL of unlabeled EGF (EGF), or increasing concentrations of EGF-750 (Labeled EGF). Lysates were probed for receptor phosphorylation using an antibody that specifically recognizes phosphorylated tyrosine 1068 of the EGFR (pY1068). Phosphorylated EGFR detected with pY1068 antibody shows only slightly diminished intensity in the cells incubated with conjugated probe at the 10 ng concentration, suggesting that the fluorescent probe retained biologic activity. Expression of EGFR was comparable for both groups, although at 100 ng/mL of EGF-750, there is some ligand-induced receptor degradation consistent with previous reports (11); α-tubulin was used as a protein loading control.

Western blot analysis

The relative expression of EGFR was evaluated in the cell lines S2VP10, S2CP9, MiaPaCa-2, PANC-1, SKOV3.ip1, NIH/3T3, and MCF7 using immunoblot analysis (Fig. 2A). Anti–β-actin antibody was used as a control for normalization in dosimetry of relative abundance. The S2VP10 line showed strong relative abundance corresponding to high EGFR overexpression, whereas MiaPaca-2 cells exhibited minimal relative abundance. Bands confirmed EGFR expression for pancreatic cell lines S2VP10, S2CP9, and PANC-1, as well as the EGFR-positive control cell line SKOV3.ip1, with dosimetry values of 1.4×, 0.6×, 0.2×, and 0.8×, respectively. No bands were detectable for the EGFR-negative cell lines NIH/3T3 and MCF7 (Fig. 2B).

Immunocytochemistry

To validate general relative efficacy of EGF in a fluorescently labeled conjugate, fixed MiaPaca-2, MCF7, and S2VP10 cells were probed with the Texas Red–EGF complex to visualize EGFR ligand–induced endocytic trafficking,

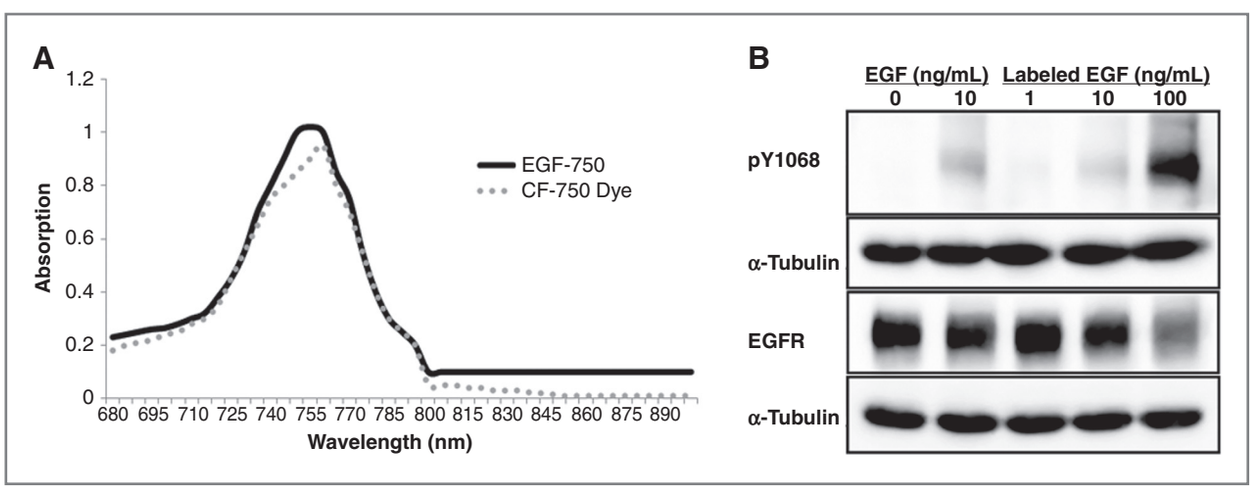

Figure 1. EGF-750 probe characterization. A, UV-Vis spectra of EGF-750 probe (black line) and CF-750 dye (dash line) measured to confirm that the absorbance signature of the dye is not significantly altered by conjugation. B, bioactivity of EGF-750 was verified by its ability to phosphorylate EGFR receptor tyrosine kinase in HeLa cells, measured by immunodetection of phosphorylated EGFR via Western blotting with pY1068 antibody. Cells treated with either unlabeled EGF (EGF) or EGF-750 (Labeled EGF) at a concentration of 10 ng/mL showed similar levels of tyrosine kinase activation of EGFR, indicating that ligand conjugation had nominal effect on probe bioactivity.

Published OnlineFirst September 12, 2014; DOI: 10.1158/0008-5472.CAN-14-1656

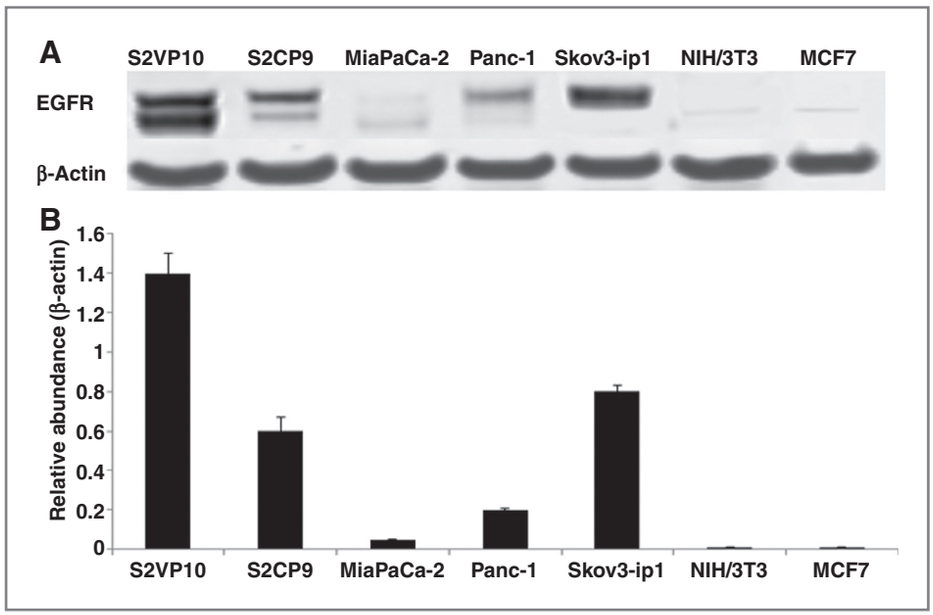

Figure 2. Expression of EGFR in pancreatic cancer cell lines. A, expression of EGFR was confirmed in S2VP10, S2CP9, MiaPaCa-2, PANC-1, and SKOV3.ip1 (EGFR-positive control) cell lines; minimal expression was detected in NIH/3T3 (EGFR-negative control) and MCF7 cells. B, dosimetry was performed using band intensity values for EGFR in comparison with actin. Values demonstrate the relative abundance of EGFR in each cell line.

measured via indirect immunofluorescence microscopy. In MiaPaca-2 and S2VP10 cell lines, conjugation of the Texas Red–EGF probe did not hinder the endocytosis of EGFR, and the MCF7 EGFR-negative cells show inconsequential staining. Intracellular indirect fluorescence of the Texas Red–EGF probe was analyzed at 0, 10, or 30 minutes; Texas Red–EGF is shown in red, EEA1 antibody in green (Fig. 3). Immunofluorescence microscopy indicated receptor distribution in cells and implied effective intracellular processing of a labeled EGF conjugate (Texas Red)-EGFR complex. Increased internalization of Texas Red–EGF in S2VP10 cells corresponded to increased levels of EGF-induced EGFR internalization with colocalization of the probe and EEA1 (27). Accumulation of probe within S2VP10 and MiaPaCa-2 cells was observed via staining of Texas Red–EGF seen at that time point. Low EGFR–expressing MCF7 cells showed minute internalization of Texas Red–EGF–EGFR complex at each time point. The addition of fluorescent dye to EGF in this case did not hinder functionality of EGF *in vitro*.

Flow cytometric analysis of EGF-750 binding

Binding specificity of EGF-750 in S2VP10 cells was quantified via flow cytometric analysis using a competitive inhibition assay. Ab-1 is a mouse monoclonal antibody to the ligand-binding domain of the EGFR and competes for ligand binding (28). NIH/3T3 cells are EGFR-negative and show little EGF-750 association; the addition of Ab-1 has little effect on EGF-750 association. In contrast, the EGFR-positive, S2VP10 cells associate with EGF-750 quite well. The addition of Ab-1 effectively blocks EGF-750's association (Fig. 4A and B). Histograms of MFI values show that the largest shift was seen in the S2VP10 line, with a 60.1% positive cell population compared with 11.1% in NIH/3T3 cells; baseline shift for each line was 2.65% and 2.59%, respectively. In cells pretreated with Ab-1 anti-EGFR antibody to block EGF receptors, EGF-750 probe signal was reduced in both S2VP10 and NIH/3T3 cells, with positive shift observed in only 23.0% and 7.18% of population, respectively. Data are representative of the mean values of two replicate experiments; differences were analyzed using the Wilcoxon signed-rank test. Although this decrease in EGF-750 probe binding is not statistically significant ($P = 0.0613$), it is a biologically significant indicator of

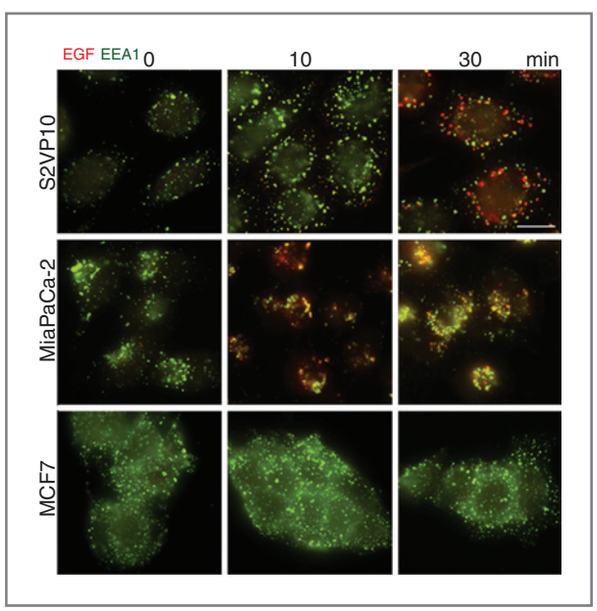

Figure 3. Uptake of the EGF-750 probe detected via immunocytochemistry. To demonstrate the retention of biopotency of EGF in a validated fluorescent probe complex, Texas Red–EGF was incubated with three pancreatic cancer cell lines and analyzed at various time points (0, 10, and 30 minutes). S2VP10 and MiaPaCa-2 cell lines show internalization of labeled EGFR–Texas Red–EGF complex (red), whereas MCF7 (low-EGFR–expressing) cells exhibit significantly reduced receptor-ligand internalization even with similar levels of endocytosis activity, apparent via labeled EEA1 antibody (green).

Published OnlineFirst September 12, 2014; DOI: 10.1158/0008-5472.CAN-14-1656

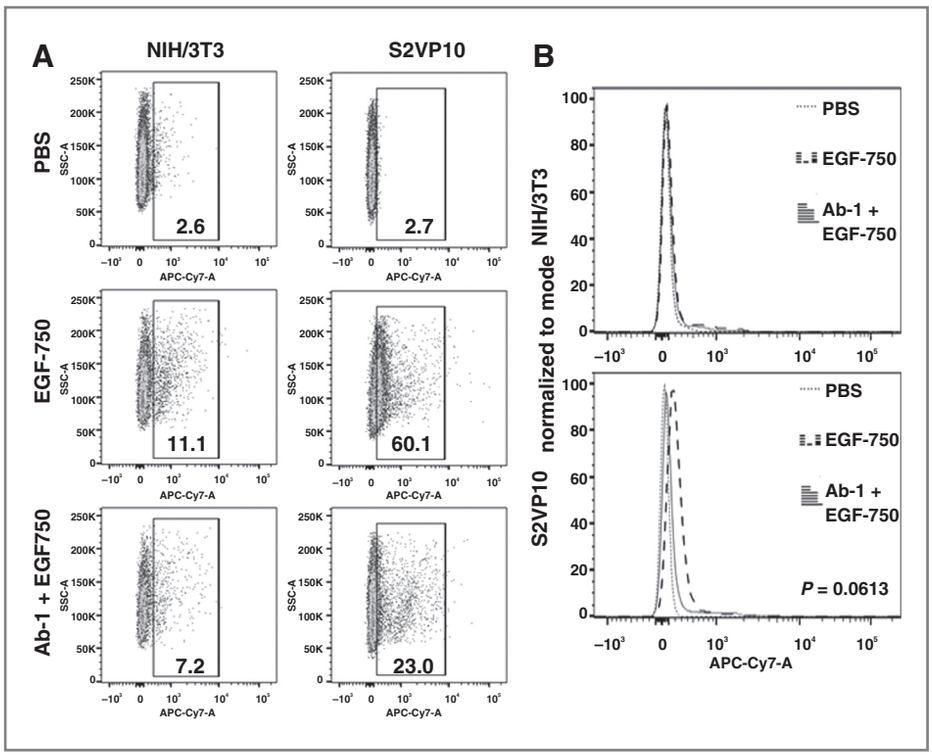

Figure 4. Extracellular accumulation of EGF-750 probe was assessed using flow cytometry. A, percentages represent proportion of APC-Cy7–positive tumor cells within gated area; values are representative of the mean of two experimental replicates. B, Wilcoxon signed-rank test determined differences in MFI was not significant among treatments ($P = 0.0613$).

binding specificity due to reduced MFI of EGF-750 probe in Ab-1–blocked cells.

Tumor imaging

Following i.v. tail vein injection of the EGF-750 probe, S2VP10L mice were imaged at 3, 6, and 24 hours postinjection. Maximum accumulation of the EGF-750 probe within tumor was recorded at the 6-hour time point, with an average of 318 MSOT signal units (arbitrary unit, a.u.; Supplementary Fig. S1). Two additional mice in cohort were imaged with similar results. MiaPaCa-2–implanted mice served as a low-EGFR–expressing tumor control; of the three mice injected, MSOT signal was <10 MSOT signal units (a.u.) for all time points. Multispectral optoacoustic tomography images of serial transversal slices from 38 to 42 mm were obtained, from the liver to the kidney, indicating a region where EGF-750 probe accumulation begins (Fig. 5A); probe intensity values indicate higher accumulation through the 40 to 42 mm slices, which represent the interior portion of the tumor mass. Maximum intensity projections show the 3D structure of the tumor in the xyz-space (Fig. 5B). Fluorescence imaging of the mice validated the accumulation of the EGF-750 probe at 6 hours with specific accumulation in the lower left quadrant of the tumor. For comparison, AMI images of CF-750 dye alone injected as a control showed no visible accumulation within the tumor at 6 hours postinjection (Fig. 5C). There was no visible probe accumulation within the kidneys or liver, suggesting that the amount was below the detection limit; MSOT output for these organs was <10 MSOT signal units (a.u.). Bioluminescent imaging was used to confirm orthotopic pancreatic tumor implantation of S2VP10L (Luc positive) cells. Tumors were localized to the pancreas with minimal metastases present (Fig. 5C). Figure 5D shows *ex vivo* pancreatic tumor and liver tissue images acquired using fluorescence imaging on the AMI to confirm specific probe uptake in the pancreas (red signal), with minimally detectable signal in the liver. *Ex vivo* scan of organs on the AMI also confirmed accumulation of EGF-750 in the pancreas contrasted with the lack of fluorescent probe distribution within the liver. Probe specificity was further implicit from the lack of accumulation of nonspecific ICG dye in MSOT images of the tumor mass following coinjection with EGF-750 probe (data not shown).

Discussion

This study demonstrates the feasibility of detecting orthotopic pancreatic cancer *in vivo* using MSOT through the active targeting of upregulated receptors with ligand-associated probes for enhanced imaging. Highly resolute, volumetric imaging revealed preferential localization of EGF-750 probe in tumor, indicating specificity in targeting and confirming that MSOT can be used to trace the biodistribution of exogenous fluorescent contrast agents through several millimeters of live tissue (Fig. 5A and B). The fluorescent receptor–targeted ligand maintained EGFR binding specificity, trafficking, and intracellular signaling activity, verifying its utility as an imaging probe for MSOT. EGF-750 demonstrated interaction with and exhibits bioactivity in association with EGFR in S2VP10 pancreatic tumor cells. Optoacoustic imaging is based on molecular light absorption induced by a tunable

Published OnlineFirst September 12, 2014; DOI: 10.1158/0008-5472.CAN-14-1656

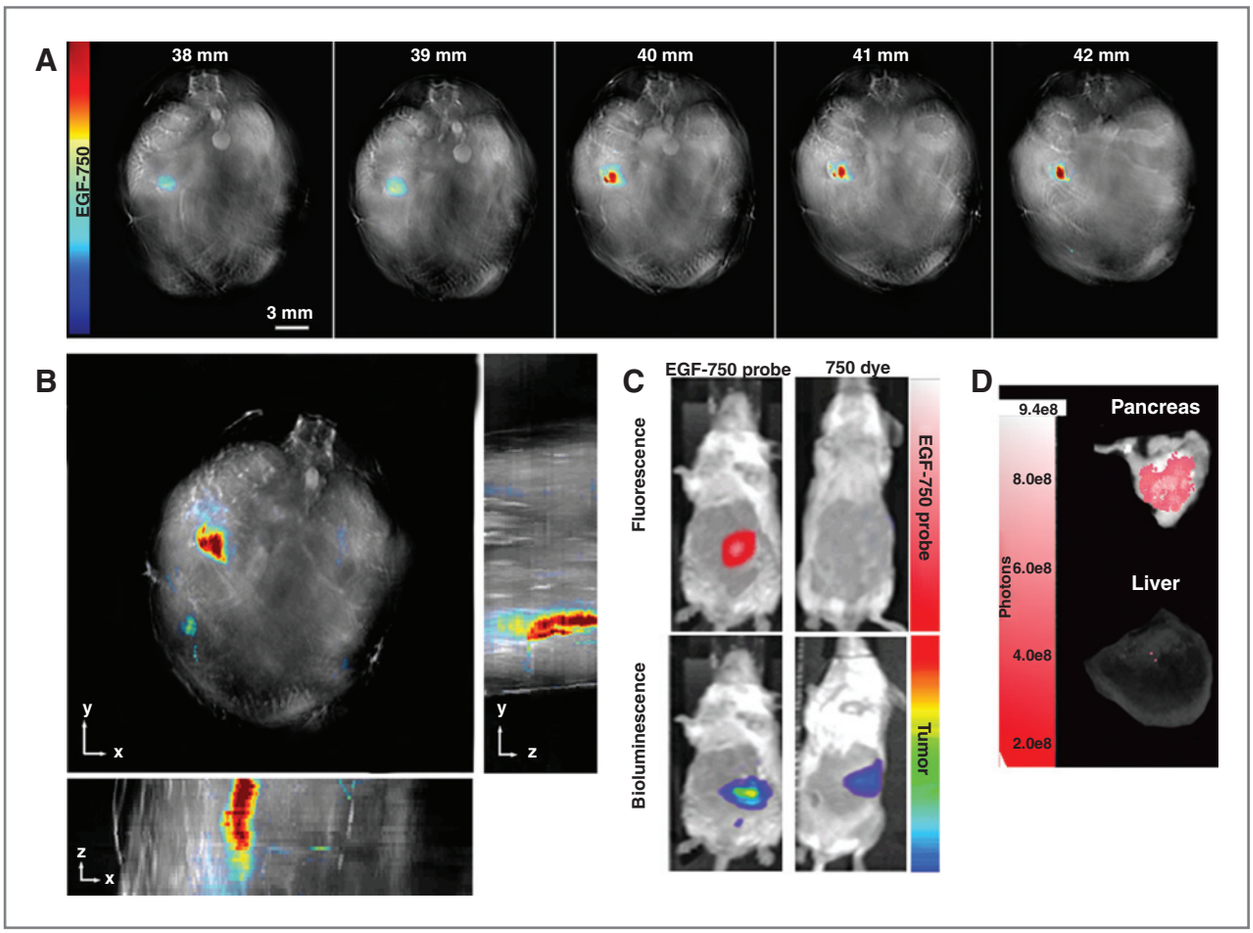

Figure 5. Optical imaging of pancreatic adenocarcinoma. Multispectral optoacoustic detection of pancreatic adenocarcinoma from a mouse at 7 days postimplantation, with EGF-750 biodistribution shown at 6 hours postinjection. High-resolution (75 μm) backprojection reconstruction and multispectral processing using linear regression in MATLAB was used to create reconstructed image. A, serial images of pancreatic tumor mass ranging from 38 to 43 mm illustrate the capability to precisely define the region of probe distribution. B, maximum intensity projection of reconstructed image to determine 3D conformation of tumor in *xyz*-space, enabling measurement of total tumor volume. C, top, fluorescence imaging of EGF-750 probe-labeled pancreatic tumor; as a control, unconjugated inert CF-750 dye was shown to not accumulate preferentially in the tumor. Bottom, detection of pancreatic tumor was confirmed using S2VP10L cells (Luc positive) through bioluminescence imaging on the AMI. D, *in vivo* MSOT images were further validated through fluorescence imaging detection of EGF-750 probe in pancreatic tumor and liver tissues analyzed *ex vivo* on the AMI; *ex vivo* scan of organs confirmed the accumulation in the pancreas and lack of fluorescent EGF-750 probe distribution in the liver, corresponding to MSOT signal quantified for the liver and kidney at <10 MSOT signal units (a.u.).

pulsed laser that delivers short pulses at wavelengths relative to selected absorbance spectra, under which conditions thermal diffusion is effectively negated, resulting in a direct proportionality of acoustic wave magnitude to the light intensity, optical absorption, and thermoelastic expansion of tissue as detected by ultrasound (29). The possibility exists for MSOT to enable fluorescent agent identification with molecular specificity at depths up to at least 2 cm. MSOT has been validated for resolution of deep-seated fluorescent proteins in *Drosophila melanogaster* pupae and adult zebrafish, and for the imaging of subcutaneous xenografts and orthotopic glioblastoma in mice (7, 30, 31). Accuracy of fluorescent probe detection is important at depth and because of light scattering in tissue; optical imaging and microscopy techniques cannot provide the image fidelity produced by multispectral optoacoustic tomography, for which sound wave-scattering in tissue is less detrimental to detection sensitivity (7, 9, 10).

Superficial tumors have been visualized using MSOT in previous studies (30, 31), although the depth range of the instrument is theoretically suitable for the detection of orthotopically implanted tumors, with the additional capacity of spectra differentiation to allow for multiparameter evaluation using several chromophores and fluorophores simultaneously. A resolution of up to 200 μm is achievable using MSOT, at depths of more than 10 transport mean free path lengths (MFPL) of photon propagation through a highly diffusing medium; that is, more than 10 times the transport length of the depth currently attainable through *in vivo* microscopy (<1 mm; refs. 7, 8). Spectral unmixing allows separation of fluorescent imaging agents from background absorption and from endogenous chromophores to depict discrete representations

Published OnlineFirst September 12, 2014; DOI: 10.1158/0008-5472.CAN-14-1656

of the tumor microenvironment, including detailed vascular anatomy. The MSOT system has been validated for detecting targeted fluorescent molecules, dyes, and accumulation of nanoparticles in the imaging of mouse mammary carcinoma allografts and orthotopic human glioblastoma xenografts (30–32). The resulting tomographic 3D images show well-defined vascular anatomy and organ specificity with optical contrast and high spatial resolution, revealing the potential to visualize orthotopic tumors such as pancreatic lesions.

There have been investigations using photoacoustic imaging models with linear array that have capability of imaging at depth but suffer from high noise level, weak signal, and long acquisition times (33). Using MSOT, photoacoustic signal is readily apparent even during image acquisition, and does not require postprocessing to identify regions of positive signal. Photoacoustic imaging without the introduction of exogenous contrast has been widely studied and shown to be useful in a variety of applications, ranging from tracking nanoparticle pharmacokinetics to hypoxic tissue detection (34, 35). We hypothesize that the introduction of exogenous contrast agents and probes could greatly enhance contrast, detection, and further enable resolution of nonsurface tumors, especially tumors located within the abdomen. Selection of the most appropriate agent for photoacoustic imaging can be challenging due to the large number of viable agents proposed for biomedical imaging (36). Photoacoustic imaging detects optical absorption in the NIR region from 650 to 1,100 nm in endogenous tissue (37). Here, we demonstrate that the EGF-750 probe is suitable for highly specific and sensitive detection of S2VP10 pancreatic tumor cells through EGF receptor targeting (Figs. 2–5).

While this study establishes a new method for detection of EGFR-expressing pancreatic adenocarcinoma with potential clinical applications, the work may be extended to the detection of other types of deep-tissue solid tumors that characteristically overexpress EGFR (38–41). The EGF-750 probe in particular could also potentially be used with a real-time handheld MSOT imaging system device (42–44) as a targeted imaging agent to identify patients who would benefit from EGFR-targeted therapeutics (45). This application could also be used to monitor treatment response or receptor sensitivity during treatment, potentially aiding in investigations of resistance to EGFR-targeted therapies (46).

Because this technique is noninvasive, longitudinal imaging is possible, enabling potential for investigations of biodistribution, pharmacokinetics, and visualization of treatment response (35). The MSOT instrument can be used for *in vivo* binding characterization and biodistribution and elimination pharmacokinetics to optimize nanovehicle targeting for anticancer therapeutics (47–49). Previous studies using MSOT have detected gold nanoparticles within subcutaneous tumors, indicating a potential role in evaluating biodistribution and accumulation of nanocarriers (32, 50). The capacity for dynamic imaging of exogenously administered targeted molecules in specific organs enables visualization and quantification of off-target binding to evaluate hepatic and renal toxicity. Future research directions include development and characterization of targeted anticancer nanotheranostics for investigations using MSOT to trace particles, imaging their transit dynamics in multiple organs, and monitoring tumor response *in vivo* at clinically relevant depths.

Disclosure of Potential Conflicts of Interest

No potential conflicts of interest were disclosed

Authors' Contributions

Conception and design: J.S. Huang, B.P. Ceresa, H.B. Frieboes, L.R. McNally
Development of methodology: S.V. Hudson, J.S. Huang, B.P. Ceresa, H.B. Frieboes, L.R. McNally
Acquisition of data (provided animals, acquired and managed patients, provided facilities, etc.): S.V. Hudson, J.S. Huang, W. Yin, S. Albeituni, J. Rush, J. Yan, B.P. Ceresa, L.R. McNally
Analysis and interpretation of data (e.g., statistical analysis, biostatistics, computational analysis): S.V. Hudson, J.S. Huang, W. Yin, S. Albeituni, A. Khanal, L.R. McNally
Writing, review, and/or revision of the manuscript: S.V. Hudson, J.S. Huang, B.P. Ceresa, H.B. Frieboes, L.R. McNally
Administrative, technical, or material support (i.e., reporting or organizing data, constructing databases): J.S. Huang, B.P. Ceresa
Study supervision: J.S. Huang, L.R. McNally

Grant Support

This study was supported by NIH grants CA139050 (L.R. McNally) and GM092874 (B.P. Ceresa)

The costs of publication of this article were defrayed in part by the payment of page charges. This article must therefore be hereby marked *advertisement* in accordance with 18 U.S.C. Section 1734 solely to indicate this fact.

Received June 4, 2014; revised August 11, 2014; accepted August 29, 2014; published OnlineFirst September 12, 2014.

References

1. Pocard M, Tsukui H, Salmon RJ, Dutrillaux B, Poupon MF. Efficiency of orthotopic xenograft models for human colon cancers. In Vivo 1996; 10:463–9.
2. Kagadis GC, Loudos G, Katsanos K, Langer SG, Nikiforidis GC. *In vivo* small animal imaging: current status and future prospects. Med Phys 2010;37:6421–42.
3. Condeelis J, Weissleder R. *In vivo* imaging in cancer. Cold Spring Harb Perspect Biol 2010;2:a003848.
4. Tangney M, Francis KP. *In vivo* optical imaging in gene & cell therapy. Curr Gene Ther 2012;12:2–11.
5. Lutzweiler C, Razansky D. Optoacoustic imaging and tomography: reconstruction approaches and outstanding challenges in image performance and quantification. Sensors 2013;13:7345–84.
6. Ntziachristos V, Razansky D. Molecular imaging by means of multispectral optoacoustic tomography (MSOT). Chem Rev 2010;110:2783–94.
7. Razansky D, Distel M, Vinegoni C, Ma R, Perrimon N, Köster RW, et al. Multispectral opto-acoustic tomography of deep-seated fluorescent proteins *in vivo*. Nat Photonics 2009;3:412–7.
8. Ntziachristos V. Going deeper than microscopy: the optical imaging frontier in biology. Nature Methods 2010;7:603–14.
9. Razansky D, Deliolanis NC, Vinegoni C, Ntziachristos V. Deep tissue optical and optoacoustic molecular imaging technologies for pre-clinical research and drug discovery. Curr Pharm Biotechnol 2012; 13:504–22.
10. Buehler A, Herzog E, Ale A, Smith BD, Ntziachristos V, Razansky D. High resolution tumor targeting in living mice by means of multispectral optoacoustic tomography. EJNMMI Res 2012;2:14.
11. Dinneen JL, Ceresa BP. Expression of dominant negative rab5 in HeLa cells regulates endocytic trafficking distal from the plasma membrane. Experimental Cell Res 2004;294:509–22.

Published OnlineFirst September 12, 2014; DOI: 10.1158/0008-5472.CAN-14-1656

12. Ceresa BP, Bahr SJ. Rab7 activity affects epidermal growth factor: epidermal growth factor receptor degradation by regulating endocytic trafficking from the late endosome. J Biol Chem 2006;281:1099–1106.
13. Ghislat G, Aguado C, Knecht E. Annexin A5 stimulates autophagy and inhibits endocytosis. J Cell Sci 2012;125:92–107.
14. Ke S, Wen X, Gurfinkel M, Charnsangavej C, Wallace S, Sevick-Muraca EM, et al. Near-infrared optical imaging of epidermal growth factor receptor in breast cancer xenografts. Cancer Res 2003;63:7870–5.
15. Sihver W, Pietzsch J, Krause M, Baumann M, Steinbach J, Pietzsch HJ. Radiolabeled cetuximab conjugates for EGFR targeted cancer diagnostics and therapy. Pharmaceuticals 2014;7:311–38.
16. Samkoe KS, Hextrum SK, Pardesi O, O'Hara JA, Hasan T, Pogue BW. Specific binding of molecularly targeted agents to pancreas tumors and impact on observed optical contrast. Proc SPIE 7568, Imaging, Manipulation, and Analysis of Biomolecules, Cells, and Tissues VIII 2010;75680H.
17. Panchuk-Voloshina N, Haugland RP, Bishop-Stewart J, Bhalgat MK, Millard PJ, Mao F, et al. Alexa dyes, a series of new fluorescent dyes that yield exceptionally bright, photostable conjugates. J Histochem Cytochem 1999;47:1179–88.
18. Hermanson GT, editor. Bioconjugate techniques, 2nd ed. London: Elsevier; 2008.
19. Hemminki A, Dmitriev I, Liu B, Desmond RA, Alemany R, Curiel DT. Targeting oncolytic adenoviral agents to the epidermal growth factor pathway with a secretory fusion molecule. Cancer Res 2001;61:6377–81.
20. Pereboeva L, Komarova S, Roth J, Ponnazhagan, Curiel DT. Targeting EGFR with metabolically biotinyated fiber-mosaic adenovirus. Gene Therapy 2007;14:627–37.
21. Leath CA III, Kataram M, Bhagavatula P, Gopalkrishnan RV, Dent P, Fisher PB, et al. Infectivity enhanced adenoviral-mediated *mda-7/IL-24* gene therapy for ovarian carcinoma. Gynecologic Oncol 2004;94:352–62.
22. Ju WD, Velu TJ, Vass WC, Papageorge AG, Lowy DR. Tumorigenic transformation of NIH 3T3 cells by the autocrine synthesis of transforming growth factor alpha. New Biol 1991;3:380–8.
23. Xu H, Yu Y, Marciniak D, Rishi AK, Sarkar FH, Kucuk O, et al. Epidermal growth factor receptor (EGFR)-related protein inhibits multiple members of the EGFR family in colon and breast cancer cells. Mol Cancer Ther 2005;4:435–42.
24. Rush JS, Ceresa BP. RAB7 and TSG101 are required for the constitutive recycling of unliganded EGFRs via distinct mechanisms. Mol Cell Endocrinol 2013;381:188–97.
25. McNally LR, Welch DR, Beck BH, Stafford LJ, Long JW, Sellers JC. KISS1 over-expression suppresses metastasis of pancreatic adenocarcinoma in a xenograft mouse model. Clin Exp Metastasis 2010;27:591–600.
26. Razansky D, Buehler A, Ntziachristos V. Volumetric real-time multispectral optoacoustic tomography of biomarkers. Nature Protocols 2011;6:1121–9.
27. Rush JS, Quinalty LM, Engelman L, Sherry DM, Ceresa BP. Endosomal accumulation of the activated epidermal growth factor receptor (EGFR) induces apoptosis. J Biol Chem 2012;287:712–22.
28. Kawamoto T, Sato JD, Le A, Polikoff J, Sato GH, Mendelsohn J. Growth stimulation of A431 cells by epidermal growth factor: identification of high-affinity receptors for epidermal growth factor by an anti-receptor monoclonal antibody. Proc Natl Acad Sci U S A 1983;80:1337–41.
29. Razansky D, Baeten J, Ntziachristos V. Sensitivity of molecular target detection by multispectral optoacoustic tomography (MSOT). Med Phys 2009;36:939–45.
30. Herzog E, Taruttis A, Beziere N, Lutich AA, Razansky D, Ntziachristos V. Optical imaging of cancer heterogeneity with multispectral optoacoustic tomography. Radiology 2012;263:461–8.
31. Burton NC, Patel M, Morscher S, Driessen WHP, Claussen J, Beziere N, et al. Multispectral opto-acoustic tomography (MSOT) of the brain and glioblastoma characterization. NeuroImage 2013;65:522–8.
32. Taruttis A, Herzog E, Razansky D, Ntziachristos V. Real-time imaging of cardiovascular dynamics and circulating gold nanorods with multispectral optoacoustic tomography. Opt Express 2010;18:19592–602.
33. Ma R, Taruttis A, Ntziachristos V, Razansky D. Multispectral optoacoustic tomography (MSOT) scanner for whole-body small animal imaging. Opt Express 2009;17:21414–26.
34. Wang X, Xie X, Ku G, Wang LV, Stoica G. Noninvasive imaging of hemoglobin concentration and oxygenation in the rat brain using high-resolution photoacoustic tomography. J Biomed Opt 2006;11:024015.
35. Taruttis A, Morscher S, Burton NC, Razansky D, Ntziachristos V. Fast multispectral optoacoustic tomography (MSOT) for dynamic imaging of pharmacokinetics and biodistribution in multiple organs. PLoS ONE 2012;7:e30491.
36. Luke GP, Yeager D, Emelianov SY. Biomedical applications of photoacoustic imaging with exogenous contrast agents. Ann Biomed Eng 2012;40:422–37.
37. Razansky D, Harlaar NJ, Hillebrands JL, Taruttis A, Herzog E, Zeebregts CJ, et al. Multispectral optoacoustic tomography of matrix metalloproteinase activity in vulnerable human carotid plaques. Mol Imaging Biol 2012;14:277–85.
38. Troiani T, Martinelli E, Capasso A, Morgillo F, Orditura M, De Vita F, et al. Targeting EGFR in pancreatic cancer treatment. Curr Drug Targets 2012;13:802–10.
39. Oliveira-Cunha M, Newman WG, Siriwardena AK. Epidermal growth factor receptor in pancreatic cancer. Cancers 2011;3:1513–26.
40. Tobita K, Kijima H, Dowaki S, Kashiwagi H, Ohtani Y, Oida Y, et al. Epidermal growth factor receptor expression in human pancreatic cancer: Significance for liver metastasis. Int J Mol Med 2003;11:305–9.
41. Bull Phelps SL, Schorge JO, Peyton MJ, Shigematsu H, Xiang LL, Miller DS, et al. Implications of EGFR inhibition in ovarian cell proliferation. Gynecol Oncol 2008;109:411–7.
42. Buehler A, Kacprowicz M, Taruttis A, Ntziachristos V. Real-time handheld multispectral optoacoustic imaging. Optics Letters 2013;38:1404–6.
43. Deán-Ben XL, Razansky D. Portable spherical array probe for volumetric real-time optoacoustic imaging at centimeter-scale depths. Optics Express 2013;21:28062–71.
44. Deán-Ben XL, Razansky D. Functional optoacoustic human angiography with handheld video rate three dimensional scanner. Photoacoustics 2013;1:68–73.
45. Cook N, Frese KK, Moore M. Assessing the role of the EGF receptor in the development and progression of pancreatic cancer. Gastrointest Cancer: Targets and Therapy 2014;4:23–37.
46. Chong CR, Jänne PA. The quest to overcome resistance to EGFR-targeted therapies in cancer. Nat Med 2013;19:1389–1400.
47. Rembielak A, Green M, Saleem A, Price P. Diagnostic and therapeutic imaging in oncology. Medicine 2011;39:693–7.
48. Kim TH, Lee S, Chen X. Nanotheranostics for personalized medicine. Expert Rev Mol Diagn 2013;13:257–69.
49. Rizzo LY, Theek B, Storm G, Kiessling F, Lammers T. Recent progress in nanomedicine: Therapeutic, diagnostic and theranostic applications. Curr Opin Biotechnol 2013;24:1159–66.
50. Bao C, Beziere N, del Pino P, Pelaz B, Estrada G, Tian F , et al. Gold nanoprisms as optoacoustic signal nanoamplifiers for *in vivo* bioimaging of gastrointestinal cancers. Small 2013;9:68–74.